



Pd nanoflakes epitaxially grown on defect MoS₂ nanosheets for enhanced nitroarenes hydrogenation to anilines

Shanhui Zhu^{a,b,*}, Zexiang Lv^{a,b}, Xiangyu Jia^{a,b}, Jiamin Wang^{a,b}, Xiaoming Li^{a,b}, Mei Dong^a, Weibin Fan^{a,**}

^a State Key Laboratory of Coal Conversion, Institute of Coal Chemistry, Chinese Academy of Sciences, Taiyuan 030001, PR China

^b University of Chinese Academy of Sciences, Beijing 100049, PR China

ARTICLE INFO

Keywords:

Pd
MoS₂
Nitroarene hydrogenation
S vacancies
Reaction mechanism

ABSTRACT

Hydrogenation of nitroarenes to anilines under mild conditions is attractive from both theoretical and practical viewpoints. Here, high-performance catalyst with layered Pd nanoparticles epitaxially growing on ultrathin MoS₂ nanosheets (Pd/MoS₂) were prepared. It shows surprisingly high catalytic activity, selectivity and stability for hydrogenation of various nitroarenes to corresponding anilines; the turnover frequency is one or two magnitudes higher than conventional Pd-based catalysts. Surface sulfur vacancies are formed on MoS₂ nanosheets with low formation energy barrier. These S vacancies provide efficient positions for adsorbing Pd atoms, which enables facile cleavage of N–O bond as result of strong interfacial electron interaction that decreases activation energy by 0.41 eV in comparison with conventional Pd catalysts. In situ spectroscopy and DFT calculation results reveal a dual-site mechanism, in which surface Pd sites adsorb and dissociate H₂ into active H*, and then readily reacts with nearby activated nitroarene to form aniline on interfacial Pd–MoS₂ sites.

1. Introduction

Nitroarene is harmful and toxic for human health, causing severe diseases such as methemoglobinemia [1,2]. The permissible exposure limit of 5 mg/m³ to human beings has been set for nitrobenzene (NB) in an 8 h-work day [1]. The strong electron affinity of –NO₂ group makes them very difficult for oxidation. Thus, catalytic reduction of nitroarenes to anilines is a promising method, because anilines are important raw materials for the production of pharmaceutical, agrochemicals, pigments, dyes and polymers [3,4]. Currently, catalytic hydrogenation of NB and its derivatives to anilines have been industrially applied on a huge scale, and a variety of Pt or Pd-based catalysts have demonstrated to be effective for this reaction [5–13]. In these catalysts, reducible metal oxides, such as TiO₂, CeO₂ or FeO_x, are usually employed as supports [5,7,9,14–17]. Atomically dispersed Pt on FeO_x shows high activity and strong chemospecificity towards the hydrogenation of functionalized nitroarenes [7]. Although some non-noble metal catalysts can activate nitroarenes, their activity and reaction rate are limited at mild conditions. Beller et al. and others reported a convenient method for preparation of stable Fe or Co oxides on carbon by pyrolysis of Fe or

Co complexes or metal-organic frameworks [18–23]. However, these catalysts are difficult to reach a turnover frequency (TOF) of 12000 mol/(mol·h) at temperature ≤ 80°C. Therefore, the intrinsic activity requests to be further improved by design of novel catalysts.

Defect engineering has been widely applied in transition metal dichalcogenides (TMDs) to tailor the electronic and geometrical factors [24–27]. Vacancies, known as a type of extremely delicate defect, are supposed to be effective and flexible in general catalytic modulation, which renders TMDs active for nitroarene reduction [28–30]. Schaak [29] fabricated WS₂ nanosheets with sulfur vacancy-rich basal planes and exhibited >99 % conversion of NB at 120 °C. Both MoS₂ [28] and MoSe₂ [30] nanosheets are also demonstrated to be effective for nitroarene reduction with NaBH₄. However, these pure TMDs showed very low intrinsic activity (< 20 mol/(mol·h)), even under high reaction temperature or using strong reducing agent. Compared to traditional three-dimensional counterparts, two-dimensional (2D) TMDs nanosheets possess abundant surface active sites and defects, which are promising positions for anchoring metal sites due to strong metal-TMD interaction. Tsang et al. reported that sulfur vacancies in MoS₂ monolayer facilitates the formation of Co–S–Mo interfacial sites that are the

* Corresponding author at: State Key Laboratory of Coal Conversion, Institute of Coal Chemistry, Chinese Academy of Sciences, Taiyuan 030001, PR China.

** Corresponding author.

E-mail addresses: zhushanhui@sxicc.ac.cn (S. Zhu), fanwb@sxicc.ac.cn (W. Fan).

<https://doi.org/10.1016/j.apcatb.2024.123958>

Received 3 January 2024; Received in revised form 29 February 2024; Accepted 14 March 2024

Available online 15 March 2024

0926-3373/© 2024 Elsevier B.V. All rights reserved.

active sites of 4-methylphenol hydrodeoxygenation [31]. These vacancies make Pt monomers still maintain atomic dispersion even though the Pt content reaches 7.5 % on the MoS₂ nanosheets [32]. These researches encourage us to use ultrathin MoS₂ 2D nanosheets with abundant S vacancies as support of metal species for catalyzing NB hydrogenation. Pure metal species, like Pd, has weak adsorption ability for NB, but is potential for activation of H₂. We attempt to design a 'dual active site' catalyst, which activates H₂ and NB at spatially separated sites.

In comparison to metal sites, interfacial sites show higher adsorption and activation ability for oxygen-containing functional groups. It has been reported that Cu–O–Zn interface sites have much higher CO₂ adsorption energy than Cu⁰ sites, indicative of a stronger activation ability for C=O groups [33,34]. The metal-support interfaces have been considered as crucial active sites in many reactions. Pt₁/α-MoC catalyst with interface structure is capable of selective hydrogenation of NB and its derivatives with high efficiency, even in the presence of CO pollutant [35]. Ultrathin MoS₂ 2D nanosheets contain abundant S vacancies and facilitate the formation of metal-support interfacial bonds. Here, layered Pd nanoparticles (NPs) are synthesized on MoS₂ nanosheets with an interfacial structure, which is highly effective for NB hydrogenation. NB adsorbed on Pd–S–Mo interfacial sites is apt to react with surface H* formed from H₂ decomposition on metallic Pd species, resulting in an extremely high NB hydrogenation activity under mild conditions.

2. Experimental

2.1. Materials

PdCl₂, NaBH₄ and Ce(NO₃)₂·6H₂O were purchased from Sinopharm Chemical Reagent Co., Ltd., China. (NH₄)₂Mo₂O₇·4H₂O and aniline were provided by Tianjin Chemical Reagent Co. Ltd, China. Thiourea was purchased from Aladdin. NaOH was purchased from Tianjin Kermel Chemical Reagent Co. Ltd, China. All the received chemicals were directly used without further purification.

2.2. Catalyst preparation

MoS₂ nanosheets were prepared by a hydrothermal method [27], in which 2 mmol (NH₄)₂Mo₂O₇·4H₂O and 28 mmol thiourea were initially mixed in 70 mL water under vigorous stirring for 10 min. Subsequently, the solution was hydrothermally treated at 220 °C for 21 h. The obtained solid was centrifuged, washed and dried at 60 °C overnight. The as-prepared MoS₂ nanosheets possessed much higher BET surface area (29.1 m²/g), while the commercially obtained bulk MoS₂ (b-MoS₂, Sinopharm Chemical Reagent Co., Ltd., China) had only 7.1 m²/g surface area.

The nanoporous Mo₂C nanowires were synthesized by a previously reported method [36]. 2.48 g (NH₄)₂Mo₂O₇·4H₂O and 3.20 g aniline were mixed in 40 mL water, followed by the addition of HCl aqueous solution (1.0 mol/L) until the formation of white precipitate at pH 4–5. After stirring at 50 °C for 6 h, the collected solid was centrifuged, washed, dried at 80 °C overnight, and annealed at 850 °C for 12 h in flowing Ar atmosphere.

CeO₂ with rod shape was prepared by a hydrothermal method. 4.5 mmol Ce(NO₃)₂·6H₂O was initially dispersed into 90 mL NaOH solution (5 mol/L) under stirring for 10 min at room temperature. Subsequently, the solid sample was centrifuged with water, dried at 80 °C overnight and calcined at 400 °C for 4 h.

For the preparation of Pd/MoS₂ catalyst (3 wt% Pd content as an example), 1 mL H₂PdCl₄ solution (0.226 mol/L) was dissolved in 10 mL H₂O under vigorous stirring, followed by the addition of 0.8 g MoS₂. After stirring for 1 h, 13.56 mL NaBH₄ (0.25 mol/L) solution was dripped into above solution with continuous stirring for 1 h. Subsequently, the solid sample was repeatedly centrifuged, washed and dried at 80 °C overnight. The other supported Pd catalysts were synthesized with the

same method as above.

2.3. Catalyst characterization

Inductively coupled plasma atomic emission spectroscopy (ICP-OES, Optima 2100DV, PerkinElmer) was conducted to measure Pd content, and their results are displayed in Table S1. N₂ adsorption–desorption isotherms were performed at –196 °C on a Micromeritics TriStar 3000 instrument. Before its measurement, the catalysts sample was pretreated at 200 °C for 8 h. X-ray powder diffractometer (XRD) was taken on Rigaku MiniFlex II desktop X-ray diffractometer using Cu Kα radiation at 40 kV and 40 mA. The images of transmission electron microscopy (TEM), high resolution TEM (HR-TEM) and high-angle annular dark-field scanning TEM (HAADF-STEM) were performed on a JEM-2011F system electron microscope at 200 kV with a field emission gun. Prior to its measurement, the sample was dispersed in ethanol by sonication, and deposited on carbon-coated copper grids. X-ray photoelectron spectroscopy (XPS) was conducted on Kratos AXIS ULTRA DLD spectrometer using Al Kα radiation. Raman spectra was performed in HORIBA Scientific LABRAM HR Evolution with an excitation wavelength of 532 nm. Electron paramagnetic resonance (EPR) spectra was measured on EMXPLUS10/12 X-band spectrometer at room temperature. In situ diffuse reflection Fourier transform infrared spectra (DRIFTS) was conducted on FTIR spectrophotometer (Nicolet Is10) using a SMART collector and an MCT detector cooled in liquid N₂. Typically, 40 mg catalyst slice was pretreated at 300 °C for 2 h in a H₂/Ar gas (20 mL/min), and subsequently cooled down into room temperature in flowing Ar gas. Once NB was introduced into the catalyst surface, DRIFTS spectra was immediately used to monitor its adsorption to saturated state. With increasing temperature to 80 °C, the adsorbed NB gradually desorbed from catalyst surface. Once the DRIFTS spectra of adsorbed NB kept stable at 80 °C, H₂ (20 mL/min) was purged into the system and the DRIFTS spectra were detected simultaneously.

2.4. Catalyst evaluation

The catalytic reactions were performed in a Teflon-lined stainless steel autoclave (NS-10–316L, Anhui Kemi Machinery Technology Co., Ltd.). 10 mmol nitrobenzene and 0.05 g catalyst were typically loaded into the reactor. After been purged with H₂ for five times, the reactor was pressured into 4.0 MPa H₂, heated to 80 °C, and kept for desired time. Once the reaction was finished, the reaction system would be rapidly cooled down in an ice-water bath. Before product analysis, the liquids products were diluted with 20 mL ethanol, and separated with catalysts by centrifugation. The collected products were analyzed by gas chromatography (GC, Shimadzu GC-2010) with a flame ionization detector using a DB-1 capillary column (60 m × 0.25 mm × 0.25 μm). All the products were identified by standard chemicals and GC-MS. For the determination of apparent activation energy and turnover frequency (TOF), the conversion of nitrobenzene was generally kept below 20 %. TOF was calculated based on surface Pd atoms, which can be obtained according to the equation that Pd dispersion multiplies by Pd amount.

$$\text{TOF} = \frac{\text{Mole number of converted nitrobenzene}}{\text{Number of surface Pd atoms} \times \text{reaction time}}$$

Pd dispersion is calculated by the equation $D = \frac{6 \times V}{a \times d}$, in which V is the volume of per Pd atom (0.0147 nm³), a is the surface area per Pd atom (0.0793 nm²), and d refers to Pd average particle size in nm from TEM counting [37].

For reusability tests, the spent catalyst was repeatedly washed with ethanol, collected by centrifugation, and dried at 80 °C overnight. Subsequently, the spent catalyst was performed according to normal procedure.

2.5. Density functional theory (DFT) calculation method

Vienna *ab initio* simulation package (VASP) was used to perform plane-wave-based periodic DFT calculations [38–40]. Perdew, Burke, and Ernzerhof (PBE) functional was employed to describe exchange and correlation energy. The electron-ion interactions were treated by projector augmented wave (PAW) setups [41,42]. According to TEM results, the most exposed Pd (1 1 1) facet was simulated with 5×5 four-layer supercell. The most exposed MoS₂ (0 0 2) surface was modelled by 5×4 three-layer supercell, in which S vacancies were built by the removal of two atoms from 20 surface S atoms on top layer to select low formation energy. The thickness of vacuum layer was 20 Å along the direction perpendicular to Pd (1 1 1) or MoS₂ (0 0 2) slabs to avoid artificial interactions between the slab and its periodic images. The Pd₁₅/MoS₂ interface was modeled with a 15 atoms Pd cluster bound to the above MoS₂ (0 0 2) model with S vacancies.

Adsorption energy (E_{ads}) was defined as the energy difference of the most stable structure, relative to clean slab (E_{slab}) and substrate molecule (E_{sub}), which is calculated by the equation $E_{\text{ads}} = E_{\text{sub/slab}} - E_{\text{slab}} - E_{\text{sub}}$. The transition states (TSs) were probed by climbing image nudged elastic band (CI-NEB) method [43,44], which were further verified by the presence of a single imaginary vibrational mode in frequency analysis. Activation energy (E_a) of an elementary reaction was defined by energy difference between TS and initial state (IS), while reaction energy (E_r) was defined by energy difference between final state (FS) and IS.

3. Results and discussions

3.1. Catalyst characterization

HR-TEM images of Pd/MoS₂ catalyst show that MoS₂ has a nanosheet morphology with a thickness of 3–5 layers (Fig. 1). The ultrathin MoS₂ nanosheet-supported Pd possessed much higher surface area than bulk MoS₂-supported Pd catalyst (Pd/b-MoS₂) (23.1 m²/g vs. 4.2 m²/g) (Table S1). A typical lattice spacing of 0.65 nm was observed in the HR-

TEM images, which is ascribed to the (002) crystalline plane of MoS₂ [27,45]. Pd NPs are uniformly dispersed on the surface of MoS₂ nanosheets (Fig. 1h), and the average particle size is about 3.0 nm (Fig. 1d). The most exposed facet of Pd NPs is (111) crystalline plane [46], as substantiated by the lattice spacing of 0.23 nm of fcc symmetry (Fig. 1b and Fig. S1). Notably, Pd species deposited on MoS₂ nanosheets formed small-layered Pd NPs, which had an average thickness of 5–8 at. layers (2–3 nm), as estimated from edge-on images of Pd NPs. Crystal structure analysis indicates that the Pd NPs strongly aligned with the (002) planes of MoS₂ support. The strong interface interaction between Pd and MoS₂ nanosheets enables Pd monomers to epitaxially grow with a relatively low speed along the direction of (111) orientation, rather than rapid aggregation to form irregular nanocrystals and random orientations [46]. The HAADF-STEM and elemental mappings confirm that Pd, S and Mo species are all homogeneously dispersed in the MoS₂ nanosheets.

Pd/b-MoS₂ shows larger Pd particle size and wider size distribution, although its Pd content is similar to that of Pd/MoS₂ (Fig. S2). This may due to a weaker interaction between Pd species and b-MoS₂. In the cases of Pd/Mo₂C and Pd/CeO₂, the Pd NPs are also highly dispersed on the supports, and thus, have small sizes (Fig. S3 and Fig. S4). No diffraction peaks characteristic of Pd species were detected by XRD technique for all the catalysts (Fig. S5). The intense diffraction peaks at 14.3°, 32.7°, 39.5°, 49.8° and 58.4° in the XRD pattern of Pd/b-MoS₂ are indexed to the (002), (100), (103), (105) and (110) crystalline planes of 2 H-MoS₂ (JCPDS No. 01-073-1508). However, these diffraction peaks were significantly broadened and became much more diffuse for Pd/MoS₂, giving another piece of evidence for considerably thinning of MoS₂ layer. Compared to conventional b-MoS₂, MoS₂ nanosheets shows a smaller 2θ value at the (002) plane diffraction peak, suggesting an expanded interlayer spacing between S–Mo–S layers, consistent with the above HR-TEM results.

Two obvious peaks centered at 380 and 407 cm^{−1} were observed in the Raman spectra (Fig. 2a). These two peaks are ascribed to the in-plane E_{2g}^1 and out-of-plane A_g^1 vibration modes of MoS₂ [24,47]. The E_{2g}^1 peak of MoS₂ nanosheets distinctly redshifted and broadened, compared to that of b-MoS₂. This indicates the softening of Mo–S phonon mode and

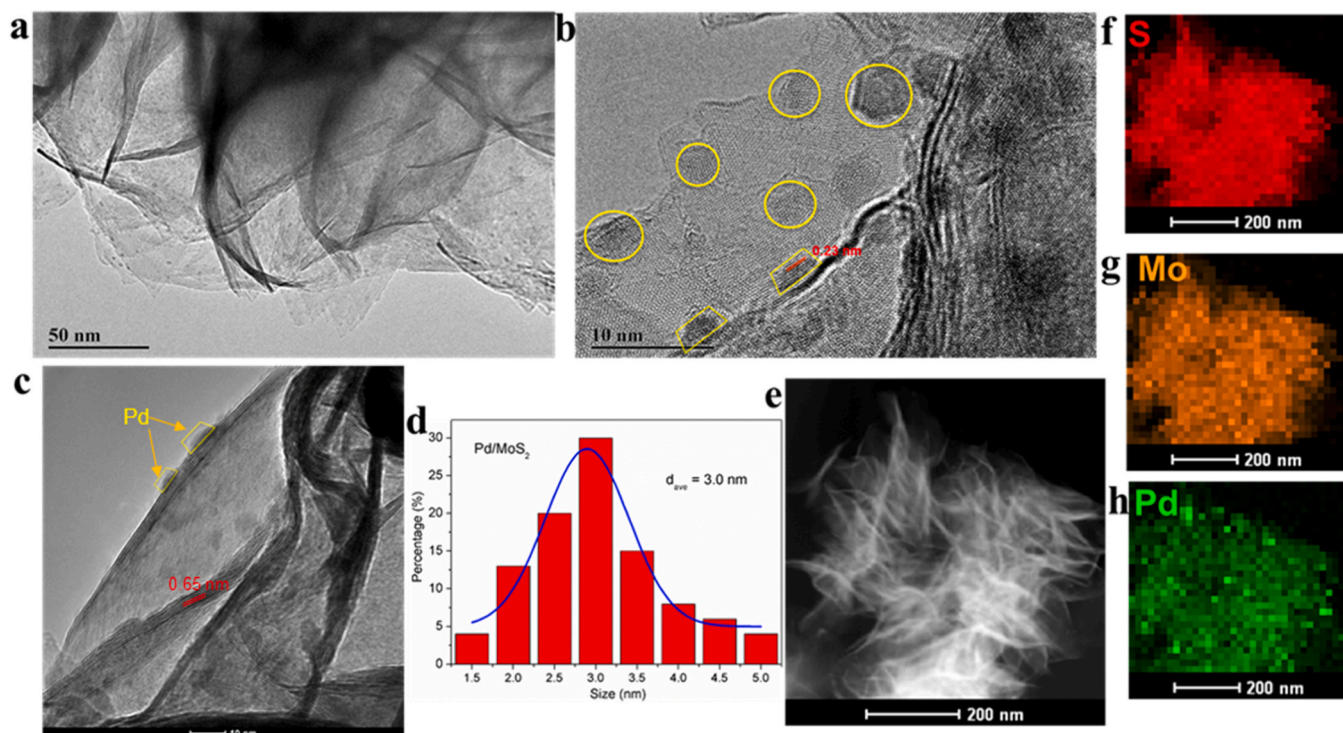


Fig. 1. (a) TEM and (b,c) HR-TEM images, (d) Pd particle size distribution, (e) HAADF-STEM image and elemental mappings of (f) S, (g) Mo and (h) Pd on Pd/MoS₂.

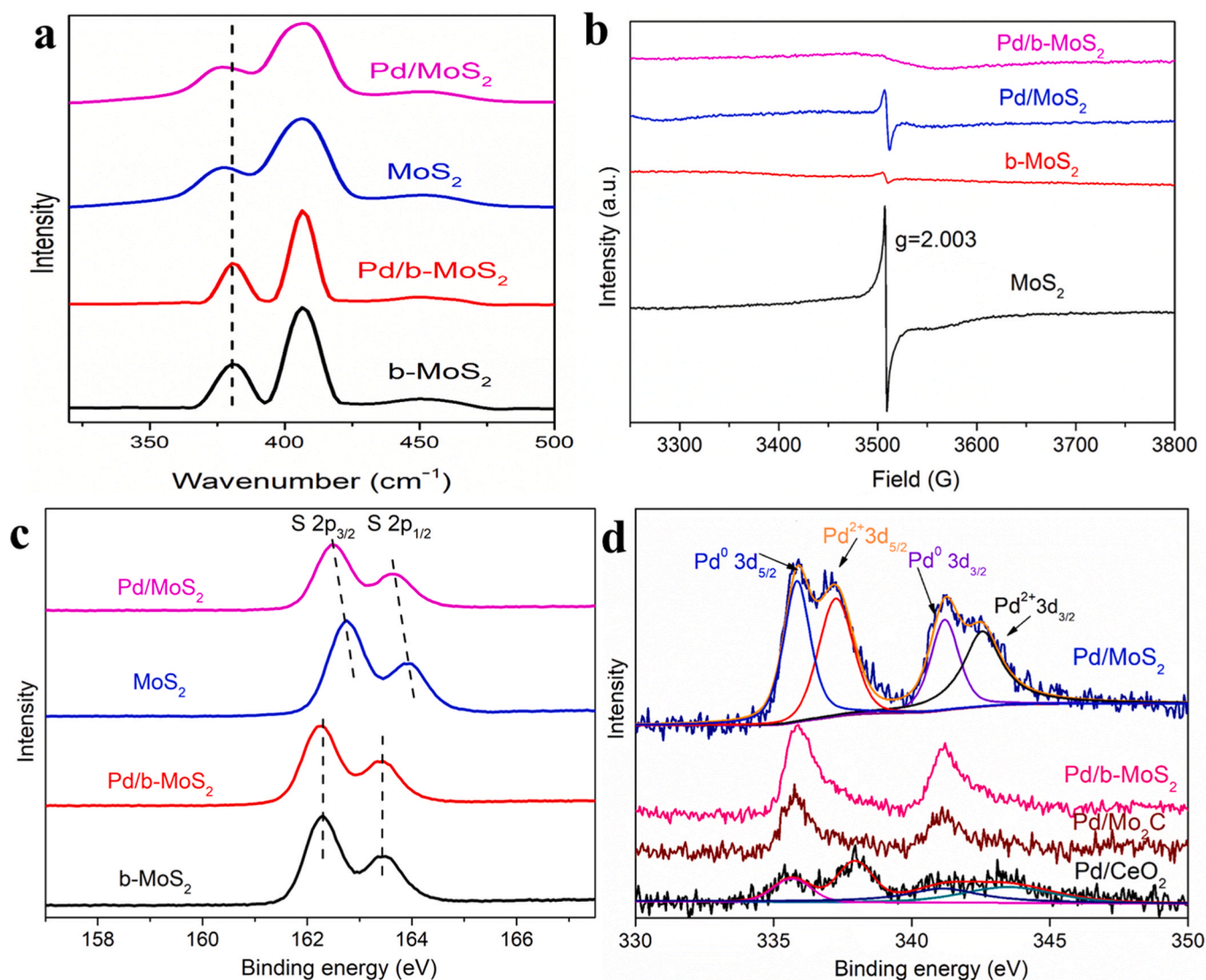


Fig. 2. (a) Raman spectra, (b) EPR spectra, and (c) S 2p and (d) Pd 3d XPS spectra of various catalysts.

basal plane, as a result of a decrease of Mo–S chemical bonds number and an increase of in-plane S vacancies. The presence of abundant S vacancies in MoS₂ nanosheets is further corroborated by the observation of an intense peak at $g = 2.003$ in its EPR spectra (Fig. 2b) [24], as this peak is corresponding to the Mo–S dangling bonds originating from the single S-vacancies on MoS₂ surface. Compared to MoS₂ nanosheets, moderate decrease of peak intensity was detected on Pd/MoS₂, suggesting that the introduced Pd species occupied some S vacancies. The very weak peaks in the EPR spectra of b-MoS₂ indicate that it has small numbers of S vacancies.

In the S 2p XPS spectra (Fig. 2c), two distinct peaks were detected at about 162.3 and 163.4 eV, which are attributed to S²⁻ in MoS₂ [26,48]. Meanwhile, two symmetrical peaks centered at 229 and 232.3 eV are assigned to Mo⁴⁺ in MoS₂ (Fig. S6) [24]. The surface S vacancy concentrations, as determined by XPS spectra in terms of the S: Mo ratio, in commercial b-MoS₂ and Pd/b-MoS₂ are 0.9 % and 0.8 %, respectively. Comparatively, those in MoS₂ nanosheets and Pd/MoS₂ reaches 12.1 % and 10.6 %, suggesting the presence of large amounts of S vacancies, consistent well with the EPR results.

In the Pd 3d XPS spectra of reduced Pd/b-MoS₂ and Pd/Mo₂C (Fig. 2d), the intense symmetrical peaks at 335.9 and 341.2 eV are assigned to Pd⁰ 3d_{5/2} and 3d_{3/2}, respectively [46,49]. Another two peaks were observed at 337.2 and 342.6 eV in the spectra of Pd/MoS₂ and

Pd/CeO₂, which are attributed to Pd²⁺ [46,49,50]. It has been reported that the presence of Pd²⁺ indicated the probable formation of Pd–O–Ce bond due to the strong interfacial interaction between Pd and CeO₂ [49]. Compared to MoS₂, addition of Pd induced a remarkable shift of S 2p peak toward low binding energy, suggesting that MoS₂ obtained electrons that probably derived from Pd. Meanwhile, the presence of Pd²⁺ peak at high binding energy was due to electron transfer from Pd⁰ into S²⁻. The XPS results confirm the existence of strong interfacial interaction between Pd species and MoS₂ nanosheets that possess a substantial number of S vacancies, and thus, facilitate the formation of interfacial Pd–S–Mo bonds.

S vacancies can be created by removing surface S atoms during DFT modelling (Fig. S7). DFT calculation results reveal that the S vacancy formation energy is 0.33 eV on MoS₂, and Pd–S–Mo bonds are formed through hybridization of Pd 3d orbitals and neighboring S 2p orbitals of MoS₂ with which can stabilize the loaded Pd on the MoS₂ surface through Pd–S interaction. The stabilization energy was calculated as high as –7.4 eV per cluster. As a result, the shift and aggregation of Pd species were prevented [51]. The optimized structure of Pd/MoS₂ is shown in Fig. 3a. The average distance of Pd–S bond is ca. 2.3 Å, giving another piece of evidence for the existence of strong interfacial interaction between interfacial Pd and S atoms. In addition, Pd atoms can partially occupy S vacancy sites to create new Pd–Mo bonds with a

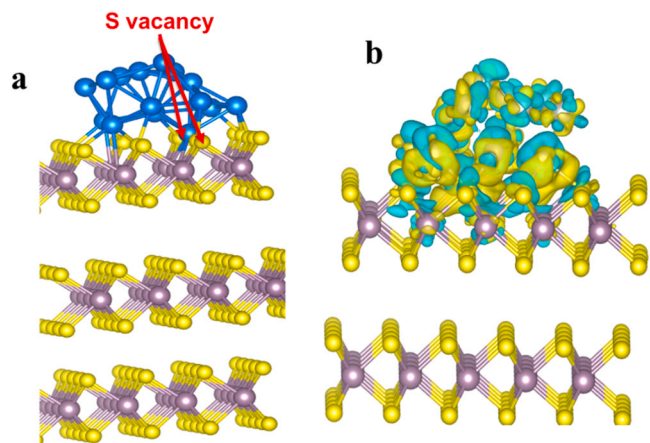


Fig. 3. (a) Atomic configuration of DFT calculation-optimized structure, and (b) calculated charge-density differences on Pd₁₅/MoS₂ model (blue, yellow, and brown balls represent Pd, S, and Mo atoms, respectively).

length of ca. 2.70 Å, consistent with ERP spectra and XPS results. In contrast, Pd clusters can only form Pd–S bonds in bulk MoS₂ with small numbers of S vacancies (Fig. S7c).

The charge density analysis can give information on the distribution

of electrons, which is readily acquired from the wave functions by DFT calculations. Charge-density differences provides direct visual evidence on electron interaction via interfacial charge transfer between different materials. The charge-density differences ($\Delta\rho$) on Pd₁₅/MoS₂ were calculated by the equation: $\Delta\rho = \rho(\text{Pd}_{15}/\text{MoS}_2) - \rho(\text{Pd}_{15}) - \rho(\text{MoS}_2)$, where $\rho(\text{Pd}_{15}/\text{MoS}_2)$, $\rho(\text{Pd}_{15})$, and $\rho(\text{MoS}_2)$ are the charge-densities of Pd₁₅/MoS₂, Pd₁₅, and MoS₂, respectively. Fig. 3b displays the charge-density differences of Pd/MoS₂ model, with yellow and blue representing charge accumulation and charge depletion, respectively. The electron densities on the interfacial Pd and MoS₂ were significantly increased and seriously overlapped between the interfaces. In addition, the subsurface Mo atoms also had electronic interaction with interfacial Pd atoms. The electron density of surface Pd species moves toward Pd–MoS₂ interface, demonstrating that the interaction between Pd clusters and surface MoS₂ sites are very strong [52]. Notably, nearly no obvious interaction is observed between Pd clusters and the subsurface MoS₂. Obviously, ultrathin nanosheet structure of MoS₂ is crucial for the formation of more Pd–MoS₂ interfacial sites due to the presence of large numbers of surface S vacancies.

3.2. Catalytic performance

Fig. 4a shows the catalytic results of various catalysts for NB hydrogenation to aniline at 80 °C and 4 MPa H₂ in the absence of solvent. Pd/b-MoS₂ and Pd/Mo₂C exhibited very low NB conversions of only 3.1

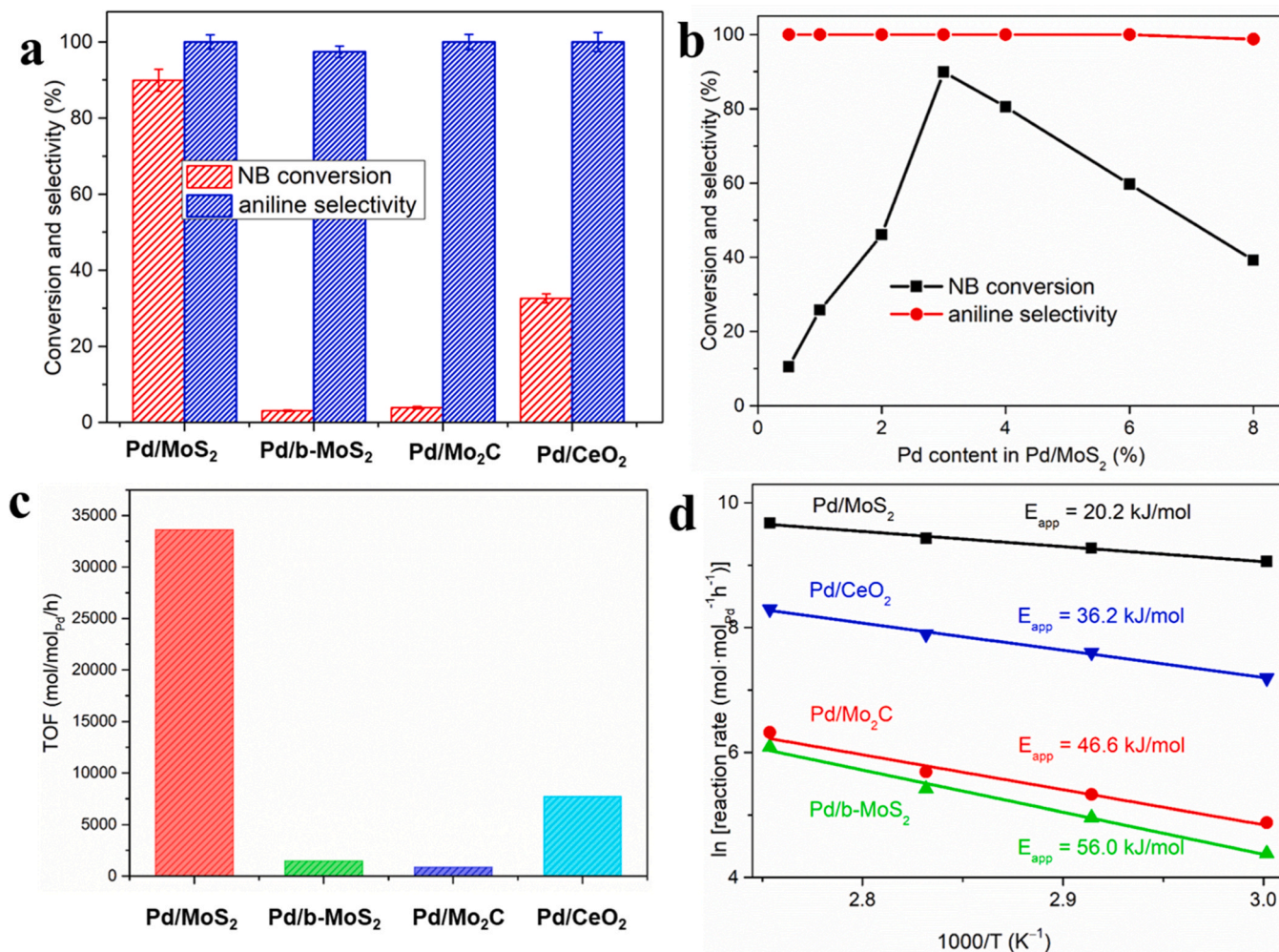


Fig. 4. (a) NB hydrogenation results over various catalysts; (b) effect of Pd content on the catalytic performance of Pd/MoS₂ for NB hydrogenation; (c) TOF value over various catalysts at 80 °C. (d) Kinetic behaviour and apparent activation energies of NB hydrogenation over various catalysts. Reaction conditions: 10 mmol NB, 0.005 g catalyst, 80 °C, 4 MPa H₂, 1 h. The reaction conditions for Fig. 4d are listed in Table S2.

% and 3.9 % respectively, whereas Pd/MoS₂ gave a NB conversion as high as 89.9 %, despite that all the catalysts displayed aniline selectivity > 97 %. The catalytic activity of MoS₂ nanosheets alone was also evaluated. However, the conversion of NB was only 0.2 %. Pd/CeO₂ is a well-known highly active catalyst for NB hydrogenation [5,53], but it also obtained low conversion (32.6 %) at the same condition, demonstrating the superior catalytic performance of Pd/MoS₂.

Fig. 4b shows that the optimal Pd content in Pd/MoS₂ catalyst is 3 wt % in theoretic content (2.59 wt% actual content by ICP). NB conversion improved with increasing Pd content from 0.5 wt% to 3 wt%. When Pd content was 3 wt%, Pd/MoS₂ achieved the best performance, up to 89.9 % NB conversion. An increase of Pd content can remarkably improve Pd active sites and promote the activity. However, too high Pd content (>3 wt%) tended to cause the agglomeration of Pd particle, decreased Pd dispersion, and thus diminished the number of interfacial Pd active sites, resulting in the decline of NB conversion. The correlation between TOF value with Pd content is displayed in Fig. S8. Similar trend was observed in the cases of TOF or NB conversion with Pd content. The TOF value also increased with Pd content, and reached the highest for 3 wt% Pd/MoS₂. The effect of reaction time on catalytic performance of NB hydrogenation was investigated on Pd/MoS₂ and the result is illustrated in Fig. S9. NB conversion gradually enhanced with increasing reaction time. Both NB conversion and aniline selectivity reached 100 % for 1.5 h.

The reusability tests of Pd/MoS₂ were performed, and the reaction result is displayed in Fig. S10a. No discernible decrease in NB conversion and aniline selectivity was observed after six recycle tests. ICP result indicated that no obvious Pd and Mo species (< 0.1 wt%) were leached into solution after reusability tests. TEM images of spent Pd/MoS₂ (Fig. S11a,b) showed that MoS₂ nanosheet structure was well maintained. The spent Pd/MoS₂ catalyst presents almost no aggregation of Pd NPs and the Pd-MoS₂ interface can still be remained. Additionally, the Raman, EPR and XPS spectra (Fig. S11c-e) of spent Pd/MoS₂ behaved similar to the fresh sample, confirming the robust chemical structure and stable S vacancies. Compared to fresh Pd/MoS₂ (52.0 %), a slight increase of Pd²⁺/(Pd⁰+Pd²⁺) ratio (55.1 %) on spent sample is probably due to Pd⁰ oxidation during post-treatment after recycle test. Because catalyst deactivation may be masked at high conversion of NB, the reusability tests were further conducted for Pd/MoS₂ at low conversion (48.9 %). Similar case (Fig. S10b) was observed that the conversion of NB and aniline selectivity was maintained within six runs, demonstrating the excellent stability of Pd/MoS₂.

The intrinsic activity of various catalysts as manifested by TOF was normalized to surface Pd. Pd/b-MoS₂ obtained a TOF value of 1461 mol/mol_{Pd}/h. Pd/CeO₂, as expected, gave a much higher TOF value of 7739 mol/mol_{Pd}/h at 80 °C, which is similar to the reported result [5,53]. Excitingly, Pd/MoS₂ displayed an extraordinarily high TOF value of 33617 mol/mol_{Pd}/h at 80 °C. To the best of our knowledge, such a TOF value has rarely been achieved [7,10,19,21,35]. It is generally one or two magnitudes higher than previously reported catalysts, and even outperforms single atom catalysts such as Pt₁/FeO_x [7], Pt₁/mpg-C₃N₄ [11], Ru₁Ni/Al₂O₃ [54], Ir₁Mo₁/TiO₂ [55] and Co₁/Graphene [56].

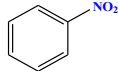
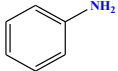
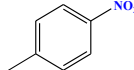
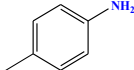
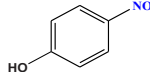
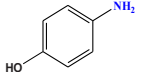
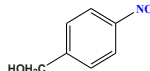
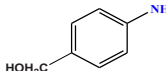
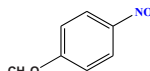
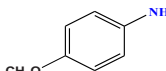
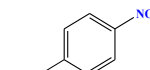
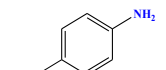
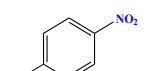
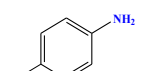
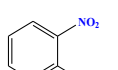
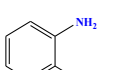
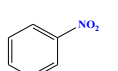
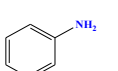
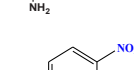
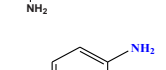
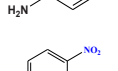
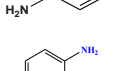
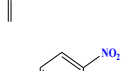
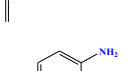
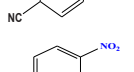
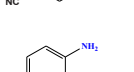
The effect of external diffusion was checked by varying the stirring speed between 600 and 1500 rpm. As shown in Fig. S12, the conversion of NB enhanced with increasing stirring speed up to 1200 rpm. However, no further enhancement of NB conversion was observed with the stirring rate of 1500 rpm. Thus, the stirring speed was fixed at 1200 rpm, which can efficiently remove the external diffusion limitation. The internal diffusion effect is mainly controlled by catalyst size. For small catalyst particle size of Pd/MoS₂ (ca. 50 μm), an inter-particle diffusion resistance can be usually excluded for tank reactor. Additionally, a further decline in particle size by grinding did not improve NB conversion, indicating the absence of internal diffusion limitations. Thus, internal and external diffusion limitations can be neglected in the intrinsic regime, and the applied reaction condition was suitable for

kinetic study. The kinetics studies (Fig. 4d and Table S2) show that the apparent activation energy (*E*_{app}) on Pd/MoS₂ is 20.2 kJ/mol, being much lower than those on Pd/b-MoS₂ (56 kJ/mol), Pd/CeO₂ (36.2 kJ/mol) and Pd/Mo₂C (46.6 kJ/mol). This accounts for the high activity of Pd/MoS₂.

The outstanding catalytic performance of Pd/MoS₂ is further substantiated by its tolerance to a variety of NB-based compounds, including both electron-donating (methyl, methoxy, and phenolic hydroxy) and electron-withdrawing (hydroxymethy, carboxyl, halogen, amino) groups-substituted NBs (Table 1). More interestingly,

Table 1

Catalytic results for hydrogenation of various substituted nitroarenes on Pd/MoS₂.

Substrate	Product	Reaction time (h)	Conv. (%)	Sel. (%)
		1.5	100	>99.9
		1.5	100	>99.9
		2	97.8	99.1
		1.5	96.5	96.9
		1.5	99.8	95.9
		2	99.6	98.7
		2	99.1	96.3
		2	96.5	98.0
		2	100	97.8
		2	99.7	96.9
		2	100	95.1
		2	100	96.8
		2	100	97.9

Reaction conditions: 10 mmol substrate, 0.005 g catalyst, 80 °C, 4 MPa H₂, 1.5 or 2 h.

nitroarenes with easily reducible alkene, nitrile and/or aldehyde functional groups can be selectively converted into corresponding anilines, although it is a challenge [18,19]. In all studied cases, the functionalized anilines selectivity is higher than 95 % along with the nitroarene conversion >96 % within 2 h.

3.3. Reaction mechanism

Fig. 5a shows the in situ DRIFTS of Pd/b-MoS₂ and Pd/MoS₂ for hydrogenation of NB at 80 °C. Two typical bands were detected at 1348 and 1527 cm⁻¹ on the both samples. These two bands are ascribed to the N=O stretching vibrations of adsorbed NB [57,58]. No significant change was observed with the reaction time on Pd/b-MoS₂, supporting its very low activity. In contrast, these two bands obviously declined at 5 min on Pd/MoS₂. Simultaneously, another two bands appeared at 1484 and 1310 cm⁻¹, which are attributed to the N=O and C–N stretching vibrations of nitrosobenzene [59]. In addition, the peaks characteristic of phenylhydroxylamine were also discerned at 1492 and 1246 cm⁻¹. Further increase of the reaction time to 30 min led to the new bands at 1622 ($\delta(\text{NH}_2)$), 1601 ($\delta(\text{NH}_2)$), 1500 ($\nu(\text{C-N})$), 1273 ($\nu(\text{C-N})$) and 1174 cm⁻¹ ($\nu(\text{C-H})$) at the expense of those for nitrosobenzene and phenylhydroxylamine. These new bands are assigned to the vibrations of adsorbed aniline [60]. The in situ DRIFTS results of Pd/MoS₂ not only demonstrate its extraordinarily high activity, but also reveal that NB is hydrogenated to aniline via the C₆H₅NO and C₆H₅NHOH intermediates (Fig. S13).

DFT calculations show that NB is very difficult to be chemically adsorbed on b-MoS₂ or MoS₂ surface (Fig. S14), but it can be adsorbed on Pd (111) plane in parallel pattern through the formation of six C–Pt bonds with an adsorption energy of –1.00 eV (Table S3). Notably, the nitro group cannot effectively bind to Pd (111) surface in a vertical way, as the adsorption energy of –0.41 eV is too weak to cause NB activation. In addition, NB can also be strongly adsorbed on Pd₁₅/MoS₂ (002) interface in parallel pattern (adsorption energy of –1.21 eV), due to the contribution from nitro group in the formation of strong N–O–Pd–S–Mo bond (Table S4). Obviously, the interfacial Pd–S–Mo bond can rapidly activate nitro group and promote its conversion. The adsorption structures of other possible intermediates were also calculated, and the results are displayed in Tables S3 and S4. Generally, their adsorption energies on Pd (111) surface are lower than those on Pd₁₅/MoS₂ interface model, which is attributed to the increased electron densities around Pd–MoS₂ interfacial area and Pd-occupied sulfur vacancies to induce electronic interaction from Pd–Mo bonds.

The H⁺ formation is vital for hydrogenation reaction [61,62]. Its rapid generation, diffusion and maximizing the coverage on active sites can greatly increase the intrinsic rate of NB reduction. H₂ dissociation is

very easy to occur on Pd (111) plane by overcoming an activation energy barrier of only 0.27 eV (Table S5). The activation energy is further decreased to 0.19 eV on Pd₁₅/MoS₂ model (Table S6), because Pd step and corner sites in Pd₁₅ cluster are more active. Notably, these surface Pd sites also display higher catalytic activity than interfacial Pd sites for H₂ activation.

In situ DRIFTS results show that NB is hydrogenated into aniline by a direct pathway as the C₆H₅NO and C₆H₅NHOH intermediates were detected. Fig. 6 and Table S5 list the related elementary reactions in detail. The C₆H₅NO₂* adsorbed on Pd (111) surface is initially hydrogenated to C₆H₅NO₂H* with an O–H bond length of 1.45 Å (TS1), which requires an activation energy barrier of 0.68 eV. The formed C₆H₅NO₂H* is further attacked by nearby H* to generate C₆H₅NO* and H₂O* with an activation energy barrier of 0.54 eV. This step is strongly exothermic with a released heat of –0.99 eV·H₂O* as a byproduct. It is weakly adsorbed on the top Pd site (adsorption energy of –0.28 eV). Thus, it can be easily desorbed from the Pd sites. The formed C₆H₅NO* species is subsequently hydrogenated into C₆H₅NHOH* by surmounting a low activation barrier of 0.52 eV. The C₆H₅NHOH* species is then sequentially hydrogenated to C₆H₅NHOH* by overcoming a high energy barrier of 0.93 eV due to serious geometric constraint effect. The formed C₆H₅NHOH* can dissociate into C₆H₅NH* and OH* by breaking robust N–O bond. This step needs to overcome a very high energy barrier of 1.25 eV and is exothermic by –0.11 eV, which is the rate-determining step. Finally, aniline is formed by the hydrogenation of C₆H₅NH* with a relatively high energy barrier of 0.85 eV. Notably, NB hydrogenation to aniline is strongly exothermic in thermodynamics, which is beneficial to achieving of high aniline selectivity.

The NB hydrogenation reaction pathway on Pd₁₅/MoS₂ interfacial model was also investigated by DFT calculations (Fig. 6 and Table S6). The activated NB is rapidly hydrogenated to C₆H₅NO₂H* with an activation energy barrier of 0.43 eV. Upon hydrogenative dehydroxylation, C₆H₅NO₂H* is transformed into C₆H₅NO* species (E_a=0.32 eV), which undergoes consecutive hydrogenation to yield C₆H₅NHOH (E_a=0.66 eV). The rate-determining step of C₆H₅NHOH* dehydroxylation requires an activation energy barrier of 0.82 eV, which is much lower than that on Pd (111) model. Unlike on Pd (111) surface, where C₆H₅NHOH* suffers a considerable rotation of N–O axes in N–OH bond scission, a small structural change at Pd₁₅/MoS₂ interface contributes to the obvious decline of activation energy. The generated C₆H₅NH* is finally hydrogenated to the aimed product of C₆H₅NH₂ by overcoming an activation energy barrier of 0.57 eV. Compared to Pd (111), Pd₁₅/MoS₂ interfacial model shows remarkably lower activation energy

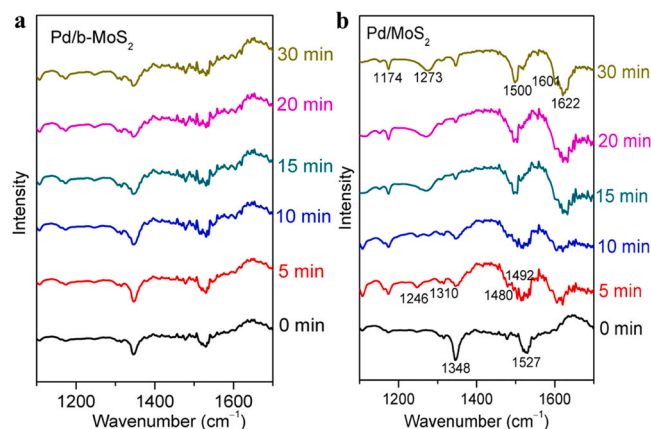


Fig. 5. In situ DRIFTS spectra of NB hydrogenation over (a) Pd/b-MoS₂ and (b) Pd/MoS₂.

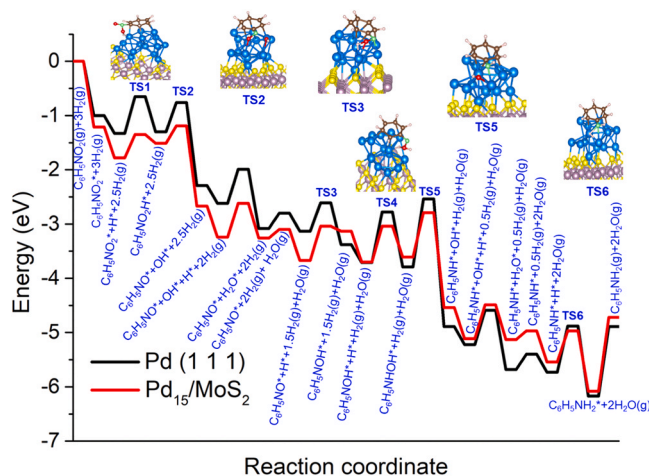


Fig. 6. Potential energy diagram for the hydrogenation of NB on Pd (111) and Pd₁₅/MoS₂. “TS” refers to the transition state. The blue, yellow, brown, black, green, red and white balls represent Pd, S, Mo, C, N, O and H atoms, respectively.

barriers in most elementary reactions, which is due to the strong interfacial interaction that increases electron density around Pd. Location of Pd atoms at the sulfur vacancies sites leads to formation of Pd–Mo bond and enhances interfacial Pd electron density. Pd–S–Mo interface bonds facilitates the adsorption and activation of N=O group, and thus, lowering its hydrogenation activation energy barrier. On Pd₁₅/MoS₂ interface, the stabilization of reaction intermediates involved in NB hydrogenation requires a synergetic action of Pd, S, and Mo sites, and the Pd–MoS₂ interface likely provides multiple active sites for the reaction.

Previous reports [11,14,58] have shown that high aniline selectivity was achieved for NB hydrogenation on noble metal catalysts. DFT calculations demonstrated that nitrobenzene is hydrogenated to produce nitrosobenzene (C₆H₅NO), hydroxylaniline (C₆H₅NHOH) and aniline successively, with strongly exothermic properties on both Pd (1 1 1) and Pd₁₅/MoS₂ models (Fig. 6). Thus, this reaction is thermodynamically driven full hydrogenation and produces aniline with high selectivity on Pd surface and Pd–MoS₂ interfacial sites.

The results of DFT calculations and in situ DRIFTS of Pd/MoS₂ for NB hydrogenation confirm that NB is hydrogenated into aniline with a direct pathway on both the Pd (111) and Pd₁₅/MoS₂ models. Notably, NB hydrogenation follows a dual-site mechanism on Pd/MoS₂, where surface Pd sites preferentially adsorb and activate H₂, while interfacial Pd–MoS₂ sites tend to activate NB molecules and promote the hydrogenation with H*. Ultrathin MoS₂ nanosheets possess large numbers of S vacancies that facilitate anchoring of Pd atoms and enhance interfacial electron interaction, and as a consequence, leading to an exciting catalytic performance.

4. Conclusions

Pd nanoflakes epitaxially grown on MoS₂ nanosheets show significantly high catalytic activity in nitroarenes hydrogenation to anilines; the TOF reaches 33617 mol/mol_{Pd}/h at 80 °C, being higher than reported values by one or two magnitudes. More interestingly, Pd/MoS₂ displays extensive substrate tolerance and excellent structural stability during recycling tests. MoS₂ nanosheets possess large numbers of sulfur vacancies as a result of low formation energy barrier of S vacancies, which have strong interfacial interactions with Pd NPs. A part of Pd atoms are adsorbed on the sulfur vacancies, forming Pd–Mo bonds. In situ DRIFTS results reveal that NB is directly hydrogenated into aniline via the formation of C₆H₅NO and C₆H₅NHOH intermediates. DFT calculations confirm that surface Pd sites can activate and dissociate H₂, whereas interfacial Pd sites facilitate NB adsorption and activation. The Pd–MoS₂ interfacial sites as main active species enable the N–O bond cleavage by decreasing the activation energy barrier of 0.41 eV. This work highlights the crucial role of sulfur vacancies in forming interfacial active sites structure and contributes to the design of high-performance supported metal catalysts.

CRedit authorship contribution statement

Weibin Fan: Writing – review & editing, Supervision, Resources, Conceptualization. **Xiangyu Jia:** Methodology, Investigation. **Jiamin Wang:** Methodology, Investigation. **Xiaoming Li:** Methodology, Investigation. **Mei Dong:** Resources, Project administration. **Shanhui Zhu:** Writing – original draft, Software, Funding acquisition, Data curation, Conceptualization. **Zexiang Lv:** Methodology, Investigation.

Declaration of Competing Interest

The authors declare that they have no known competing financial interests or personal relationships that could have appeared to influence the work reported in this paper.

Data availability

Data will be made available on request.

Acknowledgements

This work was financially supported by National Natural Science Foundation of China (22278416), Fundamental Research Program of Shanxi Province for Excellent Young Scholars (20210302122015), and ICC CAS (SCJC-DT-2023-02).

Appendix A. Supporting information

Supplementary data associated with this article can be found in the online version at doi:10.1016/j.apcatb.2024.123958.

References

- [1] C. Liu, A.-Y. Zhang, D.-N. Pei, H.-Q. Yu, Efficient electrochemical reduction of nitrobenzene by defect-engineered TiO_{2-x} single crystals, *Environ. Sci. Technol.* 50 (2016) 5234–5242.
- [2] P. Roy, A.P. Periasamy, C.-T. Liang, H.-T. Chang, Synthesis of graphene–ZnO–Au nanocomposites for efficient photocatalytic reduction of nitrobenzene, *Environ. Sci. Technol.* 47 (2013) 6688–6695.
- [3] Y. Liu, D. Han, F. Hao, W. Xiong, P. Liu, 2D-COFs-derived heteroatom-doped carbon nanosheets as high-efficiency all-solid frustrated lewis pair metal-free hydrogenation catalyst, *Appl. Catal. B: Environ.* 341 (2024) 123338.
- [4] X. Lu, J. He, L. Huang, J. Qin, Y. Ma, X. Liu, W. Zhao, B. Liu, Z. Zhang, Synergetic roles of pyridinic nitrogen and carbonyl sites in nitrogen-doped carbon for the metal-free transfer hydrogenation reactions, *Appl. Catal. B: Environ.* 324 (2023) 122277.
- [5] S. Zhang, C.R. Chang, Z.Q. Huang, J. Li, Z. Wu, Y. Ma, Z. Zhang, Y. Wang, Y. Qu, High catalytic activity and chemoselectivity of sub-nanometric Pd clusters on porous nanorods of CeO₂ for hydrogenation of nitroarenes, *J. Am. Chem. Soc.* 138 (2016) 2629–2637.
- [6] Y. Peng, Z. Geng, S. Zhao, L. Wang, H. Li, X. Wang, X. Zheng, J. Zhu, Z. Li, R. Si, J. Zeng, Pt single atoms embedded in the surface of Ni nanocrystals as highly active catalysts for selective hydrogenation of nitro compounds, *Nano Lett.* 18 (2018) 3785–3791.
- [7] H. Wei, X. Liu, A. Wang, L. Zhang, B. Qiao, X. Yang, Y. Huang, S. Miao, J. Liu, T. Zhang, FeO_x-supported platinum single-atom and pseudo-single-atom catalysts for chemoselective hydrogenation of functionalized nitroarenes, *Nat. Commun.* 5 (2014) 5634.
- [8] Y. Wang, R. Qin, Y. Wang, J. Ren, W. Zhou, L. Li, J. Ming, W. Zhang, G. Fu, N. Zheng, Chemoselective hydrogenation of nitroaromatics at the nanoscale iron (III)–OH–platinum interface, *Angew. Chem. Int. Ed.* 59 (2020) 12736–12740.
- [9] M. Macino, A.J. Barnes, S.M. Althabhan, R. Qu, E.K. Gibson, D.J. Morgan, S. J. Freakley, N. Dimitratos, C.J. Kiely, X. Gao, A.M. Beale, D. Bethell, Q. He, M. Sankar, G.J. Hutchings, Tuning of catalytic sites in Pt/TiO₂ catalysts for the chemoselective hydrogenation of 3-nitrostyrene, *Nat. Catal.* 2 (2019) 873–881.
- [10] G. Chen, C. Xu, X. Huang, J. Ye, L. Gu, G. Li, Z. Tang, B. Wu, H. Yang, Z. Zhao, Z. Zhou, G. Fu, N. Zheng, Interfacial electronic effects control the reaction selectivity of platinum catalysts, *Nat. Mater.* 15 (2016) 564–569.
- [11] S. Tian, B. Wang, W. Gong, Z. He, Q. Xu, W. Chen, Q. Zhang, Y. Zhu, J. Yang, Q. Fu, C. Chen, Y. Bu, L. Gu, X. Sun, H. Zhao, D. Wang, Y. Li, Dual-atom Pt heterogeneous catalyst with excellent catalytic performances for the selective hydrogenation and epoxidation, *Nat. Commun.* 12 (2021) 3181.
- [12] J. Zhang, L. Wang, Y. Shao, Y. Wang, B.C. Gates, F.S. Xiao, A Pd@Zeolite catalyst for nitroarene hydrogenation with high product selectivity by sterically controlled adsorption in the zeolite micropores, *Angew. Chem. Int. Ed.* 56 (2017) 9747–9751.
- [13] H. Zhang, X. Zhang, Q. Sun, Q. He, H. Ji, X. He, Boosting hydrogenation properties of Pt single-atom catalysts via tailoring the electronic structures by coordination number regulation, *Chem. Eng. J.* 455 (2023) 140808.
- [14] L. Wang, J. Zhang, H. Wang, Y. Shao, X. Liu, Y.-Q. Wang, J.P. Lewis, F.-S. Xiao, Activity and selectivity in nitroarene hydrogenation over Au nanoparticles on the edge/corner of anatase, *ACS Catal.* 6 (2016) 4110–4116.
- [15] P. Chen, A. Khetan, F. Yang, V. Migunov, P. Weide, S.P. Stürmer, P. Guo, K. Kähler, W. Xia, J. Mayer, H. Pitsch, U. Simon, M. Muhler, Experimental and theoretical understanding of nitrogen-doping-induced strong metal–support interactions in Pd/TiO₂ catalysts for nitrobenzene hydrogenation, *ACS Catal.* 7 (2017) 1197–1206.
- [16] D. González-Vera, T.M. Bustamante, J.N.D. de León, R. Dinamarca, R. Morales, P. A. Osorio-Vargas, C.C. Torres, C.H. Campos, Chemoselective nitroarene hydrogenation over Ni–Pd alloy supported on TiO₂ prepared from ilmenite-type Pd_xNi_{1-x}TiO₃, *Mater. Today Commun.* 24 (2020) 101091.
- [17] A. Shukla, R.K. Singha, S. Bhandari, V.V.D.N. Prasad, M.K. Poddar, R. Bal, Synthesis of Ni–Pd decorated spindle-shape CeO₂ for catalytic reduction of nitroarene, *Catal. Commun.* 142 (2020) 106038.
- [18] R.V. Jagadeesh, A.-E. Surkus, H. Junge, M.-M. Pohl, J. Radnik, J. Rabeah, H. Huan, V. Schünemann, A. Brückner, M. Beller, Nanoscale Fe₂O₃-based catalysts for selective hydrogenation of nitroarenes to anilines, *Science* 342 (2013) 1073–1076.

- [19] F.A. Westerhaus, R.V. Jagadeesh, G. Wienhöfer, M.-M. Pohl, J. Radnik, A.-E. Surkus, J. Rabeah, K. Junge, H. Junge, M. Nielsen, A. Brückner, M. Beller, Heterogenized cobalt oxide catalysts for nitroarene reduction by pyrolysis of molecularly defined complexes, *Nat. Chem.* 5 (2013) 537–543.
- [20] L. Liu, P. Concepción, A. Corma, Non-noble metal catalysts for hydrogenation: A facile method for preparing Co nanoparticles covered with thin layered carbon, *J. Catal.* 340 (2016) 1–9.
- [21] Peng Zhou, L. Jiang, F. Wang, K. Deng, K. Lv, Z. Zhang, High performance of a cobalt-nitrogen complex for the reduction and reductive coupling of nitro compounds into amines and their derivatives, *Sci. Adv.* 3 (2017) e1601945.
- [22] F. Zhang, C. Zhao, S. Chen, H. Li, H. Yang, X.-M. Zhang, In situ mosaic strategy generated Co-based N-doped mesoporous carbon for highly selective hydrogenation of nitroaromatics, *J. Catal.* 348 (2017) 212–222.
- [23] Z. Wei, J. Wang, S. Mao, D. Su, H. Jin, Y. Wang, F. Xu, H. Li, Y. Wang, In situ-generated Co⁰-Co₃O₄/N-doped carbon nanotubes hybrids as efficient and chemoselective catalysts for hydrogenation of nitroarenes, *ACS Catal.* 5 (2015) 4783–4789.
- [24] X. Wang, Y. Zhang, H. Si, Q. Zhang, J. Wu, L. Gao, X. Wei, Y. Sun, Q. Liao, Z. Zhang, K. Ammarah, L. Gu, Z. Kang, Y. Zhang, Single-atom vacancy defect to trigger high-efficiency hydrogen evolution of MoS₂, *J. Am. Chem. Soc.* 142 (2020) 4298–4308.
- [25] J. Hu, L. Yu, J. Deng, Y. Wang, K. Cheng, C. Ma, Q. Zhang, W. Wen, S. Yu, Y. Pan, J. Yang, H. Ma, F. Qi, Y. Wang, Y. Zheng, M. Chen, R. Huang, S. Zhang, Z. Zhao, J. Mao, X. Meng, Q. Ji, G. Hou, X. Han, X. Bao, Y. Wang, D. Deng, Sulfur vacancy-rich MoS₂ as a catalyst for the hydrogenation of CO₂ to methanol, *Nat. Catal.* 4 (2021) 242–250.
- [26] N. Luo, C. Chen, D. Yang, W. Hu, F. Dong, S defect-rich ultrathin 2D MoS₂: The role of S point-defects and S stripping-defects in the removal of Cr(VI) via synergistic adsorption and photocatalysis, *Appl. Catal. B: Environ.* 299 (2021) 120664.
- [27] J. Xie, H. Zhang, S. Li, R. Wang, X. Sun, M. Zhou, J. Zhou, X.W. Lou, Y. Xie, Defect-rich MoS₂ ultrathin nanosheets with additional active edge sites for enhanced electrocatalytic hydrogen evolution, *Adv. Mater.* 25 (2013) 5807–5813.
- [28] S. García-Dalí, J.I. Paredes, B. Caridad, S. Villar-Rodil, M. Díaz-González, C. Fernández-Sánchez, A. Adawy, A. Martínez-Alonso, J.M.D. Tascón, Activation of two-dimensional MoS₂ nanosheets by wet-chemical sulfur vacancy engineering for the catalytic reduction of nitroarenes and organic dyes, *Appl. Mater. Today* 20 (2020) 100678.
- [29] Y. Sun, A.J. Darling, Y. Li, K. Fujisawa, C.F. Holder, H. Liu, M.J. Janik, M. Terrones, R.E. Schaak, Defect-mediated selective hydrogenation of nitroarenes on nanostructured WS₂, *Chem. Sci.* 10 (2019) 10310–10317.
- [30] A. Martínez-Jódar, S. Villar-Rodil, M.A. Salvadó, D.F. Carrasco, P. Perterra, J. M. Recio, J.I. Paredes, Two-dimensional transition metal dichalcogenides beyond MoS₂ for the catalytic reduction of nitroarenes: MoSe₂ exhibits enhanced performance, *Appl. Catal. B: Environ.* 339 (2023) 123174.
- [31] G. Liu, A.W. Robertson, M.M.-J. Li, W.C.H. Kuo, M.T. Darby, M.H. Muhieddine, Y.-C. Lin, K. Suenaga, M. Stamatakis, J.H. Warner, S.C.E. Tsang, MoS₂ monolayer catalyst doped with isolated Co atoms for the hydrodeoxygenation reaction, *Nat. Chem.* 9 (2017) 810–816.
- [32] H. Li, L. Wang, Y. Dai, Z. Pu, Z. Lao, Y. Chen, M. Wang, X. Zheng, J. Zhu, W. Zhang, R. Si, C. Ma, J. Zeng, Synergistic interaction between neighbouring platinum monomers in CO₂ hydrogenation, *Nat. Nanotechnol.* 13 (2018) 411–417.
- [33] S.-S. Wang, H.-Y. Su, X.-K. Gu, W.-X. Li, Differentiating intrinsic reactivity of copper, copper-zinc alloy, and copper/zinc oxide interface for methanol steam reforming by first-principles theory, *J. Phys. Chem. C* 121 (2017) 21553–21559.
- [34] P.J.R. Shyam Kattel, Jingguang G. Chen, José A. Rodríguez, Ping Liu, Active sites for CO₂ hydrogenation to methanol on Cu/ZnO catalysts, *Science* 355 (2017) 1296–1299.
- [35] L. Lin, S. Yao, R. Gao, X. Liang, Q. Yu, Y. Deng, J. Liu, M. Peng, Z. Jiang, S. Li, Y.-W. Li, X.-D. Wen, W. Zhou, D. Ma, A highly CO-tolerant atomically dispersed Pt catalyst for chemoselective hydrogenation, *Nat. Nanotech.* 14 (2019) 354–361.
- [36] L. Liao, S. Wang, J. Xiao, X. Bian, Y. Zhang, M.D. Scanlon, X. Hu, Y. Tang, B. Liu, H. H. Girault, A nanoporous molybdenum carbide nanowire as an electrocatalyst for hydrogen evolution reaction, *Energy Environ. Sci.* 7 (2014) 387–392.
- [37] W. Luo, M. Sankar, A.M. Beale, Q. He, C.J. Kiely, P.C.A. Bruijninx, B. M. Weckhuysen, High performing and stable supported nano-alloys for the catalytic hydrogenation of levulinic acid to γ -valerolactone, *Nat. Commun.* 6 (2015) 6540.
- [38] G. Kresse, J. Hafner, Ab initio molecular dynamics for liquid metals, *Phys. Rev. B* 47 (1993) 558–561.
- [39] P.E. Blöchl, Projector augmented-wave method, *Phys. Rev. B* 50 (1994) 17953–17979.
- [40] G. Kresse, J. Furthmüller, Efficiency of ab-initio total energy calculations for metals and semiconductors using a plane-wave basis set, *Comp. Mater. Sci.* 6 (1996) 15–50.
- [41] G. Kresse, D. Joubert, From ultrasoft pseudopotentials to the projector augmented-wave method, *Phys. Rev. B* 59 (1999) 1758–1775.
- [42] J.P. Perdew, K. Burke, M. Ernzerhof, Generalized gradient approximation made simple, *Phys. Rev. Lett.* 77 (1996) 3865–3868.
- [43] G. Henkelman, B.P. Uberuaga, H. Jónsson, A climbing image nudged elastic band method for finding saddle points and minimum energy paths, *J. Chem. Phys.* 113 (2000) 9901–9904.
- [44] G. Henkelman, H. Jónsson, Improved tangent estimate in the nudged elastic band method for finding minimum energy paths and saddle points, *J. Chem. Phys.* 113 (2000) 9978–9985.
- [45] H. Fei, T. Guo, Y. Xin, L. Wang, R. Liu, D. Wang, F. Liu, Z. Wu, Sulfur vacancy engineering of MoS₂ via phosphorus incorporation for improved electrocatalytic N₂ reduction to NH₃, *Appl. Catal. B: Environ.* 300 (2022) 120733.
- [46] L. Zhou, Y. Sun, Y. Wu, Y. Zhu, Y. Xu, J. Jia, F. Wang, R. Wang, Controlled growth of Pd nanocrystals by interface interaction on monolayer MoS₂: An atom-resolved in situ study, *Nano Lett.* 23 (2023) 11360–11367.
- [47] J. Deng, H. Li, S. Wang, D. Ding, M. Chen, C. Liu, Z. Tian, K.S. Novoselov, C. Ma, D. Deng, X. Bao, Multiscale structural and electronic control of molybdenum disulfide foam for highly efficient hydrogen production, *Nat. Commun.* 8 (2017) 14430.
- [48] H. Li, S. Chen, X. Jia, B. Xu, H. Lin, H. Yang, L. Song, X. Wang, Amorphous nickel-cobalt complexes hybridized with 1T-phase molybdenum disulfide via hydrazine-induced phase transformation for water splitting, *Nat. Commun.* 8 (2017) 15377.
- [49] H. Xiong, D. Kunwar, D. Jiang, C.E. García-Vargas, H. Li, C. Du, G. Canning, X. I. Pereira-Hernandez, Q. Wan, S. Lin, S.C. Purdy, J.T. Miller, K. Leung, S.S. Chou, H.H. Brongersma, R. ter Veen, J. Huang, H. Guo, Y. Wang, A.K. Datye, Engineering catalyst supports to stabilize PdO_x two-dimensional rafts for water-tolerant methane oxidation, *Nat. Catal.* 4 (2021) 830–839.
- [50] Q. Song, W. David Wang, K. Lu, F. Li, B. Wang, L. Sun, J. Ma, H. Zhu, B. Li, Z. Dong, Three-dimensional hydrophobic porous organic polymers confined Pd nanoclusters for phase-transfer catalytic hydrogenation of nitroarenes in water, *Chem. Engineer. J.* 415 (2021) 128856.
- [51] X. Gao, S. Zhu, M. Dong, J. Wang, W. Fan, Ru/CeO₂ catalyst with optimized CeO₂ morphology and surface facet for efficient hydrogenation of ethyl levulinate to γ -valerolactone, *J. Catal.* 389 (2020) 60–70.
- [52] L. Lin, W. Zhou, R. Gao, S. Yao, X. Zhang, W. Xu, S. Zheng, Z. Jiang, Q. Yu, Y.-W. Li, C. Shi, X.-D. Wen, D. Ma, Low-temperature hydrogen production from water and methanol using Pt/ α -MoC catalysts, *Nature* 544 (2017) 80–83.
- [53] X. Shi, X. Wang, X. Shang, X. Zou, W. Ding, X. Lu, High performance and active sites of a ceria-supported palladium catalyst for solvent-free chemoselective hydrogenation of nitroarenes, *ChemCatChem* 9 (2017) 3743–3751.
- [54] W. Liu, H. Feng, Y. Yang, Y. Niu, L. Wang, P. Yin, S. Hong, B. Zhang, X. Zhang, M. Wei, Highly-efficient RuNi single-atom alloy catalysts toward chemoselective hydrogenation of nitroarenes, *Nat. Commun.* 13 (2022) 3188.
- [55] J. Fu, J. Dong, R. Si, K. Sun, J. Zhang, M. Li, N. Yu, B. Zhang, M.G. Humphrey, Q. Fu, J. Huang, Synergistic effects for enhanced catalysis in a dual single-atom catalyst, *ACS Catal.* 11 (2021) 1952–1961.
- [56] H. Yan, X. Zhao, N. Guo, Z. Lyu, Y. Du, S. Xi, R. Guo, C. Chen, Z. Chen, W. Liu, C. Yao, J. Li, S.J. Pennycook, W. Chen, C. Su, C. Zhang, J. Lu, Atomic engineering of high-density isolated Co atoms on graphene with proximal-atom controlled reaction selectivity, *Nat. Commun.* 9 (2018) 3197.
- [57] T.-N. Ye, Y. Lu, J. Li, T. Nakao, H. Yang, T. Tada, M. Kitano, H. Hosono, Copper-based intermetallic electride catalyst for chemoselective hydrogenation reactions, *J. Am. Chem. Soc.* 139 (2017) 17089–17097.
- [58] J. Luo, A. Huang, Y.-Y. Yang, X.-Y. Ma, Q.-L. Chen, J. Chen, Y. Wu, Pd/Co catalyst with high Pd atom utilization efficiency for nitrobenzene hydrogenation at room temperature: Experimental and DFT studies, *Chem. Eur. J.* 29 (2023) e202203142.
- [59] G. Richner, J.A. van Bokhoven, Y.-M. Neuhold, M. Makosch, K. Hungerbühler, In situ infrared monitoring of the solid/liquid catalyst interface during the three-phase hydrogenation of nitrobenzene over nanosized Au on TiO₂, *Phys. Chem. Chem. Phys.* 13 (2011) 12463–12471.
- [60] A. Corma, P. Concepción, P. Serna, A different reaction pathway for the reduction of aromatic nitro compounds on gold catalysts, *Angew. Chem. Int. Ed.* 46 (2007) 7266–7269.
- [61] P. Liu, Y. Zhao, R. Qin, S. Mo, G. Chen, L. Gu, D.M. Chevrier, P. Zhang, Q. Guo, D. Zang, B. Wu, G. Fu, N. Zheng, Photochemical route for synthesizing atomically dispersed palladium catalysts, *Science* 352 (2016) 797–800.
- [62] K. Lee, P.C.D. Mendes, H. Jeon, Y. Song, M.P. Dickieson, U. Anjum, L. Chen, T.-C. Yang, C.-M. Yang, M. Choi, S.M. Kozlov, N. Yan, Engineering nanoscale H supply chain to accelerate methanol synthesis on ZnZrO_x, *Nat. Commun.* 14 (2023) 819.